Rapid Communications

Bethe-Slater-curve-like behavior and interlayer spin-exchange coupling mechanisms in two-dimensional magnetic bilayers

Cong Wang,[1] Xieyu Zhou,[1] Linwei Zhou,[1] Yuhao Pan,[1] Zhong-Yi Lu,[1] Xiangang Wan,[2] Xiaoqun Wang,[3] and Wei Ji[1,*]

[1]*Beijing Key Laboratory of Optoelectronic Functional Materials & Micro-Nano Devices, Department of Physics, Renmin University of China, Beijing 100872, People's Republic of China*

[2]*National Laboratory of Solid State Microstructures and School of Physics, Nanjing University, Nanjing 210046, People's Republic of China*

[3]*Department of Physics and Astronomy, Collaborative Innovation Center of Advanced Microstructures, Shanghai Jiao Tong University, Shanghai 200240, People's Republic of China*

(Received 27 September 2019; revised 26 May 2020; accepted 3 June 2020; published 6 July 2020)

Layered magnets have recently received tremendous attention, however spin-exchange coupling mechanism across their interlayer regions is yet to be revealed. Here, we report a Bethe-Slater-curve (BSC)-like behavior in *nine* transition metal dichalcogenide bilayers (MX_2, M = V, Cr, Mn; X = S, Se, Te) and established interlayer spin-exchange coupling mechanisms at their van der Waals gaps using first-principle calculations. The BSC-like behavior offers a distance-dependent interlayer antiferromagnetic (AFM) to ferromagnetic (FM) transition. This phenomenon is explained with the spin-exchange coupling mechanisms established using bilayer $CrSe_2$ as a prototype in this work. The Se p_z wave functions from two adjacent interfacial Se sublayers overlap at the interlayer region. The spin alignment of the region determines interlayer magnetic coupling. At a shorter interlayer distance, Pauli repulsion at the overlapped region dominates and thus favors antiparallel oriented spins leading to interlayer AFM. For a longer distance, kinetic-energy gain of polarized electrons across the bilayer balances the Pauli repulsion and the bilayer thus prefers an interlayer FM state. In light of this, the AFM-FM transition is a result of competition between Pauli and Coulomb repulsions and kinetic-energy gain. All these results open a route to tune interlayer magnetism and the revealed spin-exchange coupling mechanisms are paramount additions to those previously established ones.

DOI: 10.1103/PhysRevB.102.020402

Two-dimensional (2D) magnetism has received increasing attention after demonstrations of ferromagnetism (FM) in 2D layers [1–7]. While each magnetic few-layer consists of strong covalently bonded monolayers, their interlayer couplings are governed by much weaker noncovalent, e.g., van der Waals (vdW), interactions at their "vdW gaps", which show even more interesting and mysterious magnetic behaviors [1,8–10]. Bilayer CrI_3 is one of the most popular magnetic few-layers, in which local magnetic moments (3.28 μ_B/Cr) [10] form an intralayer FM order below 45 K [1,8]. However, its interlayer magnetic coupling is variable between FM and antiferromagnetism (AFM) depending on local stacking geometry, highlighting the importance of interlayer magnetic couplings in 2D magnetism [8,10]. There are numbers of previously well-established spin-exchange coupling mechanisms for classic magnetism, e.g., superexchange in a linear (AFM) [11] and a perpendicular (FM) [12] configuration, double exchange (FM) [13,14], direct exchange (AFM/FM) [15,16], and Ruderman-Kittel-Kasuya-Yosida interactions (AFM/FM) [17–20]. While these mechanisms were derived mostly on the basis of covalently and/or metallically bonded bulk solids, knowledge is still lacking of those for noncovalent interactions at, e.g., vdW gaps which are yet to be unveiled.

Strength of interlayer interactions at vdW gaps was previously thought rather weak but was recently found to be appreciably strong in terms of modifying electronic structures and related physical properties [9,21–25]. In a significant portion of 2D layers, interlayer wave functions, as driven by dispersion attraction, do overlap and hybridize to release Pauli and Coulomb repulsions [9,21–25]. Charge redistribution induced by this interaction is relatively small at the vdW gap of a CrI_3 bilayer [10] in comparison with other bilayers like BP [21,22], Te [23,26], $PtSe_2$ [24], PtS_2 [25], and CrS_2 [9], suggesting a limited overlap of interlayer wave functions in the CrI_3 bilayer. It is exceptional that such a small overlap could even appreciably affect the interlayer magnetism through direct exchange between two interlayer I atoms separated by 4.20 Å [10]. A question then arises of how do strongly overlapped interlayer wave functions affect interlayer magnetism and whether there are any generalized spin-exchange coupling mechanisms solely for such a noncovalent interaction.

Here, we found a Bethe-Slater-curve (BSC) [27–30]-like behavior at the vdW gaps of *nine* transition metal dichalcogenide bilayers (TMDC, MX_2, M = V, Cr, Mn; X = S, Se, Te) using density functional theory (DFT) and unveiled two spin-exchange coupling mechanisms, together with a modified Hubbard model to understand such behavior. In particular, each of these bilayers prefers interlayer AFM at shorter interlayer distances and favors FM at elongated distances.

*Corresponding author: wji@ruc.edu.cn

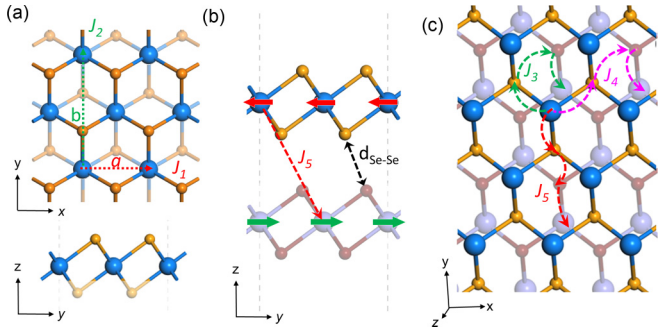

FIG. 1. Atomic structures of $CrSe_2$ mono- and bilayers. (a) Top and side views of a $CrSe_2$ monolayer. Dodger-blue, solid, and semitransparent orange balls represent Cr and top and bottom Se atoms, respectively. Red and green dashed arrows denote intralayer spin-exchange parameters J_1 and J_2 between Cr sites, corresponding to lattice constants a and b. (b) Side view of an AA-stacked $CrSe_2$ bilayer. Green and red arrows represent magnetization directions of Cr atoms. Violet and dark red balls represent Cr and Se atoms in the bottom layer, respectively. The red dashed arrow indicates exchange pathway J_5. The black arrow represents the interlayer Se-Se distance d_{Se-Se}. (c) Top oblique view of bilayer $CrSe_2$ explicitly shows three exchange pathways of J_3, J_4, and J_5 with green, pink, and red dashed arrows.

The AFM-FM transition was found to be determined by a competition between Pauli (Coulomb) repulsion at the interlayer region and kinetic-energy gain across the entire bilayer. This behavior and the explanation are general for different chalcogen and/or transition metal atoms.

We use $CrSe_2$ as a prototypic TMDC in this work. Its monolayer takes a hexagonal 1T structure with the P-3M1 space group [Fig. 1(a)], which is an analog of the strongly interlayer-coupled CrS_2 layers [9], but offers better synthetic feasibility [31,32]. Computational details can be seen in the method part of the Supplemental Material [33] (see also Refs. [21–25,34–48] therein). Its FM order is metastable with an optimized lattice constant of $a = 3.42$ Å and magnetic moment of $M = 3.09\,\mu_B$/Cr (Fig. S1 and Table S1 of the Supplemental Material [33]). The ground state is, however, striped AFM (sAFM-ABAB, Fig. S2c [33]) in a $1 \times \sqrt{3}$ orthorhombic lattice with slightly expanded $a = 3.50$ Å, largely shrunk $b = 5.63$ Å, and nearly unchanged $M = 3.02\,\mu_B$/Cr; see Table S1 [33] for details. Competition of in-plane spin-exchange parameters $J_1 = -2.32$ meV and $J_2 = -0.91$ meV leads to the sAFM-ABAB ground state. In a $CrSe_2$ bilayer, the AA stacking [Figs. 1(b) and 1(c)] is over 13.9 meV/Cr more stable than the AB stacking (Fig. S3 and Table S2 [33]) and was chosen for further discussion. It undergoes an intralayer sAFM-to-FM transition in the bilayer ($J_1 = 7.70$ meV and $J_2 = 1.60$ meV), ascribed to the strong interlayer wave-function overlap induced Cr e_g-to-t_{2g} charge transfer and its resulting intralayer double-exchange mechanism [9]. This strong coupling is confirmed by a reduced monolayer thickness of ~0.2 Å, a ~ $0.1\,\mu_B$/Cr enhanced magnetic moment, and a large interlayer binding energy $E_b = -0.32$ eV/formula unit(f.u.) (see Table S1 [33]). While bilayer CrS_2 shows interlayer FM, interlayer AFM configuration in bilayer $CrSe_2$ is 1.16 meV/Cr more favored than the interlayer FM. This unexpected interlayer AFM is determined by parameters $J_3 - J_5$ [Figs. 1(b) and 1(c) and Table S1 [33]). Although parameter J_3 has the nearest interlayer Cr-Cr distance of 5.67 Å, the farthest (8.31 Å) parameter $J_5 = -1.25$ eV, however, yields the strongest AFM coupling strength while $J_3 = 0.95$ eV and $J_4 = 0.90$ eV show weaker FM couplings. All these results suggest the $CrSe_2$ bilayer deserves a closer examination.

The interlayer magnetism of the $CrSe_2$ bilayer strongly depends on vertical sliding, while laterally sliding in a CrI_3 bilayer allows tuning its interlayer magnetism between AFM and FM [10,49,50]. Figure 2(a) plots the interlayer AFM-FM energetic difference as a function of the interlayer Se-Se distance [$d_{Se\text{-}Se}$, Fig. 1(b)], which shows a Bethe-Slater-curve (BSC)-like [27–30] behavior at the vdW gap. The BSC was used to explain different magnetic orderings of metals, e.g., Cr [51], Ni [52], Fe [53]. All considered functionals and vdW correction methods [38–40,42–47] exceptionally show that interlayer AFM and FM are favored at shorter and longer distances, respectively, although different functionals slightly affect the AFM-FM transition distance (d_T) (Table S5 [33]). Particularly, PBE predicts $d_T = 3.45$ Å while HSE06 defers it by 0.05 Å. Spin-orbit coupling (SOC) reduces the energy difference by 1–2 meV/Cr but keeps d_T nearly unchanged [Fig. 4(a) and Table S5 [33]). Effects of magnetic anisotropy energies (MAEs) were also considered that are one order of magnitude smaller than the AFM-FM energy differences, which unlikely influence the ground state of a certain bilayer (Table S6 [33]).

Figure 2(b) plots the U dependence of distance-dependent FM-AFM energy differences and Table S7 [33] summarizes the dependence of d_T and magnetic moments. A smaller U value of 2.0–4.0 eV shortens d_T, however a larger U value of 5.0–6.0 eV entirely eliminates the FM region and enlarges the energy difference by 2.01 meV/Cr and magnetic moment of $0.05\,\mu_B$/Cr at the equilibrium distance (d_E). Although d_T depends on the U value, the transition behavior is well reproduced by the HSE06 functional [green circles in Fig. 2(a) and purple stars in Fig. 2(b)], which is usually believed to better predict magnetic properties than DFT+U methods do. Here, the linear-response method [48] deriving $U = 4.5$ eV gives the upper limit of U. We are thus confident to claim the BSC-like behavior in the $CrSe_2$ bilayer. This U-value dependent d_T suggests the transition is, most likely, relevant with Coulomb and Pauli interactions and electron kinetic energy because of their U dependence in DFT calculations.

While the in-plane orbitals of Se primarily determine the intralayer magnetism, the out-of-plane Se $4p_z$ orbitals may play a paramount role in interlayer magnetism. We thus focus on the role of Se $4p_z$ orbitals. In the $CrSe_2$ bilayer, two interfacial Se $4p_z$ orbitals overlap and hybridize into one bonding and one antibonding state (Fig. S4 [33]). We mapped the wave-function norm of this bonding state on the atomic structure in Fig. 3(a) where an explicit overlapped region (OR) is evidenced at the interlayer area, which could be effectively considered as an area accumulating appreciable shared charge from the two interfacial Se sublayers.

In the interlayer FM configuration [Figs. 3(b)–3(f)], interfacial Se (Se_it, Se_ib) $4p_z$ orbitals significantly overlap [denoted by curved short-dashed lines in Figs. 3(b) and 3(c)],

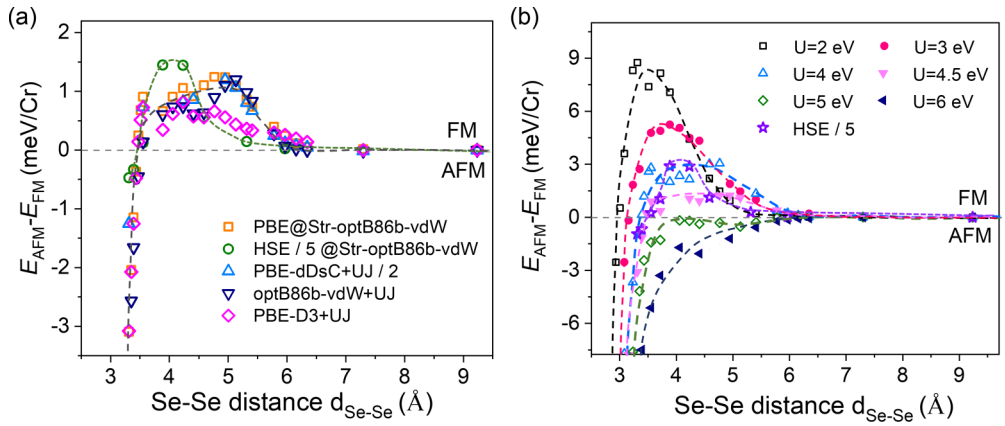

FIG. 2. Bethe-Slater-curve-like behavior in bilayer $CrSe_2$. (a) Total-energy differences between the interlayer AFM/FM configurations as a function of interlayer Se-Se distance $d_{Se\text{-}Se}$ [marked with black arrow in Fig. 1(b)] for the $CrSe_2$ bilayer calculated using different functionals. Here, PBE and HSE06 energies were compared based on optB86b-vdW relaxed structures. Energy differences for the PBE-dDsC+UJ and the HSE06 results are plotted with scaling factors of $1/2$ and $1/5$, respectively. (b) FM-AFM energy differences evolution with different on-site U values with a constant J value of 0.6 eV. The HSE06 results were plotted for reference.

leading to charge transfers of the spin-1 (up) component from interfacial Se $4p_z$ to Cr t_{2g} [indicated by curved red solid arrows in Fig. 3(b)]. As a result, the third Cr_bot (top) t_{2g} orbital becomes partially occupied [Fig. 3(c)] and the averaged local magnetic moment of Cr enlarges by $0.05\,\mu_B$, see Table S1 [33], which lead to the intralayer sAFM to FM transition from monolayer to bilayer through Cr-Cr double exchange, similar to the CrS_2 case [9]. Those charge transfers are supported by differential charge density (DCD) plots (Fig. S5 [33]). In addition, the transferred spin-1 (spin-up for simplification

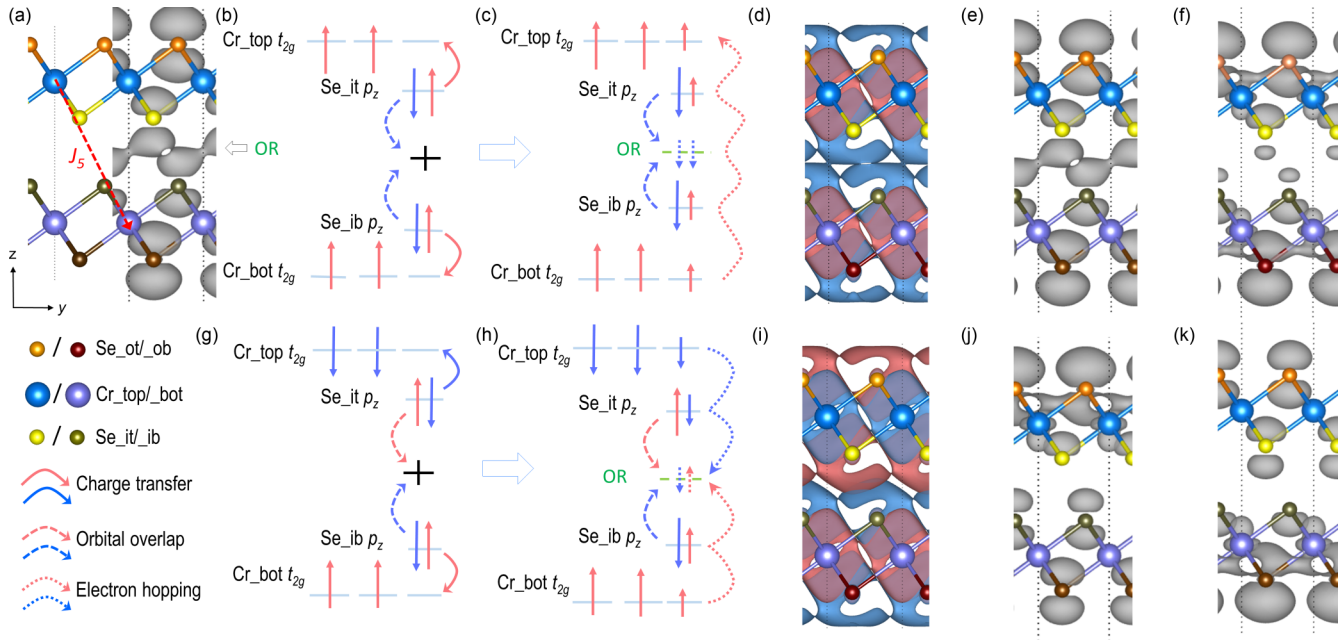

FIG. 3. Spin-exchange coupling mechanisms of the $CrSe_2$ bilayer. (a) Side view of bilayer $CrSe_2$ with indicative of spin-exchange coupling J_5 and mapped with the wave-function norms of the Se $4p_z$ bonding state where an overlapped region (OR) was identified. Atoms at different positions are marked with different colors. Panels (b) and (g) are schematics of the interlayer charge transfer and wave-function overlaps and (c) and (h) illustrate spin-exchange mechanisms of the interlayer FM (b), (c) and AFM (g), (h) configurations, respectively. Spin-up and -down electrons are represented by red straight-up and blue straight-down arrows, the length of which qualitatively represents the amount of spin-polarized electrons. Red (spin-up) and blue (spin-down) curved arrows indicate the charge transfer (solid), wave-function overlap (dashed), and electron hopping (dotted), respectively. Spin densities of the both configurations were plotted in (d) and (i), respectively, with an isosurfacevalue of $0.0004\,e/\text{Bohr}^3$. Red and blue contours denote spin-up and -down, respectively. The maximum value of the spin density is $0.6\,e/\text{Bohr}^3$, locating at the Cr site. Panels (e), (f) and (j), (k) visualize the wave-function norms of the spin-down (e), (j) and -up (f), (k) components of the interfacial bonding states for both interlayer FM (e), (f) and AFM (j), (k), respectively. An isosurface value of $0.0015\,e/\text{Bohr}^3$ was used.

hereinafter) charge of Se p_z to Cr leaves the spin-2 (spin-down hereinafter) component predominated at the OR, as shown in Figs. 3(e) and 3(f) and illustrated in Fig. 3(c).

We then focus on its interlayer spin-exchange coupling mechanism for J_5, as depicted in Fig. 3(c). The third t_{2g} orbitals of both Cr_top and Cr_bot are spin-up polarized and partially occupied. The spin-up electrons of Cr_bot t_{2g}, for example, could hop into the Se_ib $4p_z$ orbital and then reach the OR upon excitation because they are spin-down polarized and still allow spin-up electrons to occupy. Given the same reason, the electron could go further from the OR to Cr_top t_{2g} through Se_it $4p_z$, as denoted by the wavelike red dotted arrow; this substantially lowers the kinetic energy of spin-up electrons across the bilayer. This process is similar to double exchange but is mediated by multiple sites. We thus termed it "multi-intermediate double exchange." However, we should notice that the OR are effectively filled with two spin-down fractional electrons, which violates the Pauli exclusion law if OR is a real atomic site, giving rise to an appreciable Pauli repulsive interaction (P). We used a modified interlayer Hubbard model to describe it as follows:

$$\mathrm{H} = -\sum_{i,j,\sigma=\downarrow,\uparrow} t_{ij}(C^{+}_{i\sigma}C_{j\sigma} + \mathrm{H.c.}) + \sum_{i} U_i n_{i\uparrow} n_{i\downarrow} + \sum_{\sigma=\downarrow,\uparrow} P_\sigma n_{or\_t,\sigma} n_{or\_b,\sigma},$$

where the first and second terms are hopping and on-site Coulomb contributions of the conventional Hubbard model and the third term represents Pauli repulsion at the OR (more strictly, between the two p_z orbitals of Se_it and Se_ib). Here, i and j span all four atomic sites, i.e., Cr_top (bot) and Se_it(b), while the Pauli term is for the OR solely and $n_{\mathrm{or\_}t(\mathrm{or\_}b),\sigma}$ represents spin-dependent occupation at the OR contributed from Se_it (ib), see Supplemental Material Note 1 [33] (see, also, Refs. [54,55] therein) for details. In other words, the third Pauli term accounts for the Pauli repulsive energy between the overlapped p_z wave fucntions of Se_ib and Se_it. Because the $CrSe_2$ bilayer is metallic for the interlayer direction (Fig. S7 [33]), it was usually believed that $t > U$. If Pauli repulsion P could be further surmounted by hopping t, the interlayer FM configuration is still favored, otherwise, an interlayer AFM configuration is suggested.

The AFM bilayer also has the stacking induced charge transfer and the interfacial wave-function overlap, but both spin components are involved [Fig. 3(g)]. Thus, the overlapped wave function at the OR is composed of both spin components [Figs. 3(h)–3(k)]. Charge transfers occurring in the bottom and top $CrSe_2$ layers [denoted by solid arrows in Fig. 3(g)] give rise to more strongly polarized Cr_bot and Cr_top t_{2g} orbitals, antiparallel polarized Se_it and Se_ib $4p_z$ orbitals, and the nonpolarized OR, respectively, as illustrated in Fig. 3(h) and depicted by spin density in Fig. 3(i) and spin-dependent wave-function norms in Figs. 3(j) and 3(k). Figure 3(h) shows two major differences for the AFM spin-exchange coupling mechanism from the FM one. The spin-nonpolarized OR indicates that Pauli repulsion P is largely eliminated, which substantially lowers the total energy of the bilayer. However, such configuration shortens the range that a spin-polarized electron can move across the bilayer. We use a spin-down electron of Cr_top t_{2g} (in blue) as an example. It could hop into the Se_it $4p_z$ site and then to the OR, similar to the FM case, but further hopping to the Se_ib $4p_z$ site is forbidden because its spin-down component is fully occupied; this appreciably lifts up the kinetic energy. Again, if the lowered potential energy by eliminating Pauli repulsion overcomes the risen kinetic energy, AFM is thus preferred as the interlayer magnetic ground state.

In short, competition between the interlayer hopping (t) across the bilayer and the Pauli (P) and Coulomb (U) repulsions at the OR determines the interlayer magnetism of $CrSe_2$, resulting in the BSC-like behavior (Fig. 2). This phenomenological picture is supported by the calculations of the interlayer-distance dependent exchange-splitting (Coulomb), bandwidth (hopping), and spin-polarized electron-density (Pauli) of the interfacial Se p_z orbitals (Fig. S6 [33]). At shorter distances, the FM state shows largely reduced exchange splitting of the p_z orbital, increased density of the same spin component at the OR, and slightly enlarged bandwidth of the interlayer bonding state. All these results prefer the AFM state. Nevertheless, it is prone to favor FM with increasing interlayer distance. An enlarged U value localizes electrons and thus reduces the role of kinetic energy but enhances that of Pauli repulsion, more preferring interlayer AFM, consistent with our results shown in Fig. 2(b). At d_T of bilayer $CrSe_2$, the more predominant Pauli repulsion finds the interlayer AFM ground state with 0.05 Å shorter interlayer distance and 0.01 eV larger interlayer binding energy.

We extended our discussion to CrS_2 and $CrTe_2$ bilayers. Figure 4(a) plots the energy-distance relations of CrX_2 (X = S, Se, Te) revealed using HSE06(-SOC), each of which follows the expected BSC-like behavior with different d_T values. The d_T of 2.74 Å for CrS_2 is 0.46 Å shorter than its d_E of 3.20 Å, at which it nearly yields the largest energy difference, consistent with the strong FM in the literature [9]. Although d_T of $CrTe_2$ depends on the functional or U value adapted or whether SOC was considered [Fig. 4(b) and Table S8 [33]], the smallest predicted d_T is 4.22 Å, much larger than its d_E of 3.62 Å, implying the interlayer AFM in a broad spectrum of distance. Competition between Pauli and Coulomb repulsions results in this element-dependent transition-equilibrium distances relation, the details of which are discussed in Figs. S7 and S8, and Tables S3 and S8 [33] (see, also, Refs. [56–60] therein). We further generalized the BSC-like behavior to VX_2 [6] and MnX_2 [4,61] bilayers, all of which follow our expectation [Figs. 4(c) and S8 [33]). The BSC-like behavior maintains even when a monoclinic 1T" phase [60], as a special case, was considered for VTe_2 (Fig. S9 and Table S4 [33]), suggesting the robustness of this behavior.

In summary, we proposed a modified Hubbard model to explain the interlayer FM and AFM ground states for nine MX_2 (M = V, Cr, Mn; X = S, Se, and Te) bilayers at different distances. Each of these bilayers contains an interlayer wave-function overlapped region. Competition between Pauli and Coulomb repulsions at this region and kinetic-energy gain across the bilayer leads to the BSC-like behaviors, i.e., distance-dependent AFM-FM transition, in all considered MX_2 bilayers. Differently from the BSC behavior in 3D magnetic materials, only a 0.05 Å increase of inter-

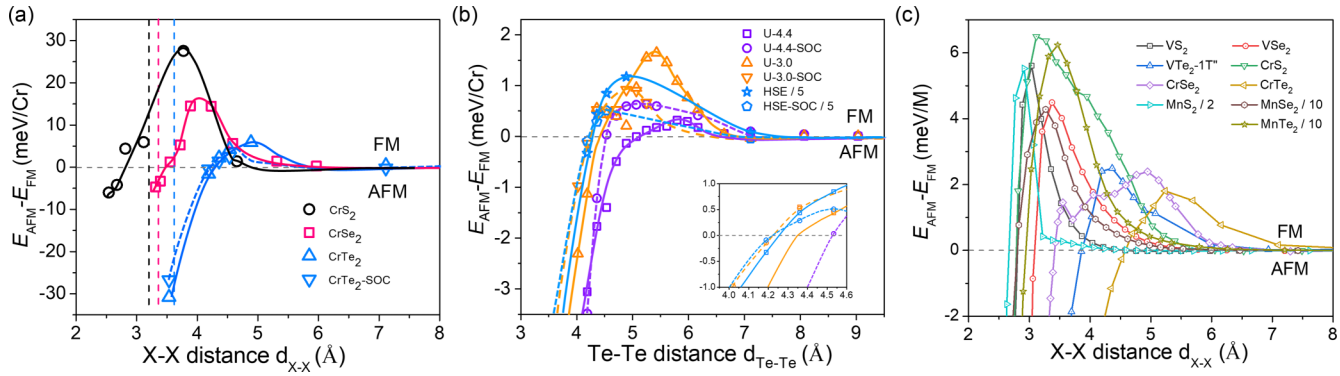

FIG. 4. Generalization of Bethe-Slater-curve-like behavior. (a) Distance dependent FM-AFM energy differences revealed with HSE06 for CrS_2 (black), $CrSe_2$ (red), and $CrTe_2$ (blue) bilayers. Equilibrium positions of CrS_2, $CrSe_2$, and $CrTe_2$ are marked with black, red, and blue dashed vertical lines. (b) Comparison of the BSC-like curves revealed with different on-site U values with the HSE06 ones for bilayer $CrTe_2$. All SOC results were shown in dashed lines while results without SOC are represented by solid lines. (c) AFM-FM energy differences for MX_2 (M = V, Cr, Mn; X = S, Se, Te) bilayers calculated with PBE-dDsC+UJ (see Table S9 [33] for structural details).

layer distance, with an energy cost of tens of meV, could induce the AFM to FM transition, illustrating the feasibility of tuning magnetism by changing interlayer distance. While "multi-intermediate double exchange" was termed for the interlayer FM coupling, for the interlayer AFM coupling, we could regard the X_it-OR-X_ib group as a superorbital and M_top and M_bot atoms couple through this "superorbital mediated superexchange" mechanism. We can infer that these two interlayer magnetic coupling mechanisms also work for other strongly electronic coupled 2D magnetic layers in which S, Se, or Te atoms sit between their vdW gaps, like Fe_3GeTe_2 and $MnBi_2Te_4$. In addition, these mechanisms also suggest a giant magnetoelastic effect in 2D layers where a small interlayer vertical displacement changes the total magnetism.

Note added. Recently, we became aware that an extended superexchange mechanism was proposed to address the magnetism in bulk Ca_3LiOsO_6 [62], which is essentially similar to our proposed superorbital mediated superexchange. We thank Dr. Y. Guo for bringing this reference to us.

We gratefully acknowledge financial support from the Ministry of Science and Technology (MOST) of China (Grant No. 2018YFE0202700), the National Natural Science Foundation of China (Grants No. 11622437, No. 61674171, and No. 11974422), the Strategic Priority Research Program of Chinese Academy of Sciences (Grant No. XDB30000000), the Fundamental Research Funds for the Central Universities, China, and the Research Funds of Renmin University of China [Grants No. 16XNLQ01 and No. 19XNQ025 (W.J.), and No. 19XNH065 (X.Z.)]. C.W. was supported by the Outstanding Innovative Talents Cultivation Funded Programs 2017 of Renmin University of China. Calculations were performed at the Physics Lab of High-Performance Computing of Renmin University of China, Shanghai Supercomputer Center.

C.W. and X.Z. contributed equally to this work.

[1] B. Huang, G. Clark, E. Navarro-Moratalla, D. R. Klein, R. Cheng, K. L. Seyler, D. Zhong, E. Schmidgall, M. A. McGuire, and D. H. Cobden *et al.*, Layer-dependent ferromagnetism in a van der Waals crystal down to the monolayer limit, Nature (London) **546**, 270 (2017).

[2] K. S. Burch, D. Mandrus, and J.-G. Park, Magnetism in two-dimensional van der Waals materials, Nature (London) **563**, 47 (2018).

[3] C. Gong and X. Zhang, Two-dimensional magnetic crystals and emergent heterostructure devices, Science **363**, eaav4450 (2019).

[4] M. Bonilla, S. Kolekar, Y. Ma, H. C. Diaz, V. Kalappattil, R. Das, T. Eggers, H. R. Gutierrez, M.-H. Phan, and M. Batzill, Strong room-temperature ferromagnetism in VSe2 monolayers on van der Waals substrates, Nat. Nanotechnol. **13**, 289 (2018).

[5] Y. Deng, Y. Yu, Y. Song, J. Zhang, N. Z. Wang, Z. Sun, Y. Yi, Y. Z. Wu, S. Wu, and J. Zhu *et al.*, Gate-tunable room-temperature ferromagnetism in two-dimensional Fe_3GeTe_2, Nature (London) **563**, 94 (2018).

[6] D. J. O'Hara, T. Zhu, A. H. Trout, A. S. Ahmed, Y. K. Luo, C. H. Lee, M. R. Brenner, S. Rajan, J. A. Gupta, and D. W. McComb *et al.*, Room temperature intrinsic ferromagnetism in epitaxial manganese selenide films in the monolayer limit, Nano Lett. **18**, 3125 (2018).

[7] C. Gong, L. Li, Z. Li, H. Ji, A. Stern, Y. Xia, T. Cao, W. Bao, C. Wang, and Y. Wang *et al.*, Discovery of intrinsic ferromagnetism in two-dimensional van der Waals crystals, Nature (London) **546**, 265 (2017).

[8] D. R. Klein, D. MacNeill, J. L. Lado, D. Soriano, E. Navarro-Moratalla, K. Watanabe, T. Taniguchi, S. Manni, P. Canfield, and J. Fernández-Rossier *et al.*, Probing magnetism in 2D van der Waals crystalline insulators via electron tunneling, Science **360**, 1218 (2018).

[9] C. Wang, X. Zhou, Y. Pan, J. Qiao, X. Kong, C.-C. Kaun, and W. Ji, Layer and doping tunable ferromagnetic order in two-dimensional CrS_2 layers, Phys. Rev. B **97**, 245409 (2018).

[10] P. Jiang, C. Wang, D. Chen, Z. Zhong, Z. Yuan, Z.-Y. Lu, and W. Ji, Stacking tunable interlayer magnetism in bilayer CrI_3, Phys. Rev. B **99**, 144401 (2019).

[11] P. W. Anderson, Antiferromagnetism. Theory of superexchange interaction, Phys. Rev. **79**, 350 (1950).

[12] W. Geertsma and D. Khomskii, Influence of side groups on 90° superexchange: A modification of the Goodenough-Kanamori-Anderson rules, Phys. Rev. B **54**, 3011 (1996).

[13] P. W. Anderson and H. Hasegawa, Considerations on double exchange, Phys. Rev. **100**, 675 (1955).

[14] P. G. de Gennes, Effects of double exchange in magnetic crystals, Phys. Rev. **118**, 141 (1960).

[15] T. Kai, H. Fujiwara, T. C. Schulthess, and W. H. Butler, First principles study of direct exchange coupling between the grains in NiMn antiferromagnets, J. Appl. Phys. **89**, 7940 (2001).

[16] A. J. Freeman and R. E. Watson, Theory of direct exchange in ferromagnetism, Phys. Rev. **124**, 1439 (1961).

[17] J. R. Schrieffer and P. A. Wolff, Relation between the Anderson and Kondo Hamiltonians, Phys. Rev. **149**, 491 (1966).

[18] P. Bruno and C. Chappert, Oscillatory Coupling between Ferromagnetic Layers Separated by a Nonmagnetic Metal Spacer, Phys. Rev. Lett. **67**, 1602 (1991).

[19] B. Heinrich and J. F. Cochran, Ultrathin metallic magnetic films: Magnetic anisotropies and exchange interactions, Adv. Phys. **42**, 523 (1993).

[20] F. Matsukura, H. Ohno, A. Shen, and Y. Sugawara, Transport properties and origin of ferromagnetism in (Ga,Mn)As, Phys. Rev. B **57**, R2037(R) (1998).

[21] Z.-X. Hu, X. Kong, J. Qiao, B. Normand, and W. Ji, Interlayer electronic hybridization leads to exceptional thickness-dependent vibrational properties in few-layer black phosphorus, Nanoscale **8**, 2740 (2016).

[22] J. Qiao, X. Kong, Z.-X. Hu, F. Yang, and W. Ji, High-mobility transport anisotropy and linear dichroism in few-layer black phosphorus, Nat. Commun. **5**, 4475 (2014).

[23] J. Qiao, Y. Pan, F. Yang, C. Wang, Y. Chai, and W. Ji, Few-layer Tellurium: one-dimensional-like layered elementary semiconductor with striking physical properties, Sci. Bull. **63**, 159 (2018).

[24] Y. Zhao, J. Qiao, Z. Yu, P. Yu, K. Xu, S. P. Lau, W. Zhou, Z. Liu, X. Wang, W. Ji *et al.*, High-electron-mobility and air-stable 2D layered $PtSe_2$ FETs, Adv. Mater. **29**, 1604230 (2016).

[25] Y. Zhao, J. Qiao, P. Yu, Z. Hu, Z. Lin, S. P. Lau, Z. Liu, W. Ji, and Y. Chai, Extraordinarily strong interlayer interaction in 2D layered PtS_2, Adv. Mater. **28**, 2399 (2016).

[26] C. Wang, X. Zhou, J. Qiao, L. Zhou, X. Kong, Y. Pan, Z. Cheng, Y. Chai, and W. Ji, Charge-governed phase manipulation of few-layer tellurium, Nanoscale **10**, 22263 (2018).

[27] J. C. Slater, Atomic shielding constants, Phys. Rev. **36**, 57 (1930).

[28] J. C. Slater, Cohesion in monovalent metals, Phys. Rev. **35**, 509 (1930).

[29] A. Sommerfeld and H. Bethe, in *Aufbau Der Zusammenhängenden Materie*, edited by A. Smekal (Springer, Berlin, 1933), p. 333.

[30] R. Cardias, A. Szilva, A. Bergman, I. D. Marco, M. I. Katsnelson, A. I. Lichtenstein, L. Nordström, A. B. Klautau, O. Eriksson, and Y. O. Kvashnin, The Bethe-Slater curve revisited; new insights from electronic structure theory, Sci. Rep. **7**, 4058 (2017).

[31] C. F. van Bruggen, R. J. Haange, G. A. Wiegers, and D. K. G. de Boer, CrSe, a new layered dichalcogenide, Physica B+C **99**, 166 (1980).

[32] Q. Tang, C. Liu, B. Zhang, and W. Jie, Synthesis of sub-micro-flakes $CrSe_2$ on glass and (110) Si substrates by solvothermal method, J. Solid State Chem. **262**, 53 (2018).

[33] See Supplemental Material at http://link.aps.org/supplemental/10.1103/PhysRevB.102.020402 for the theoretical methods, the modified interlayer Hubbard model to describe the spin-exchange coupling mechanism, geometric and magnetic details of mono- and bilayer MX_2, calculations of spin-exchange parameters, illustration and definition of the overlapped region, interlayer differential charge density, the interlayer distance dependent hopping, Coulomb and Pauli repulsion, effect of U values and functionals, magnetic anisotropy energies, and adopted on-site Coulomb U and exchange J.

[34] P. E. Blöchl, Projector augmented-wave method, Phys. Rev. B **50**, 17953 (1994).

[35] G. Kresse and D. Joubert, From ultrasoft pseudopotentials to the projector augmented-wave method, Phys. Rev. B **59**, 1758 (1999).

[36] G. Kresse and J. Furthmüller, Efficiency of ab-initio total energy calculations for metals and semiconductors using a plane-wave basis set, Comput. Mater. Sci. **6**, 15 (1996).

[37] G. Kresse and J. Furthmüller, Efficient iterative schemes for ab initio total-energy calculations using a plane-wave basis set, Phys. Rev. B **54**, 11169 (1996).

[38] K. Lee, É. D. Murray, L. Kong, B. I. Lundqvist, and D. C. Langreth, Higher-accuracy van der Waals density functional, Phys. Rev. B **82**, 081101(R) (2010).

[39] M. Dion, H. Rydberg, E. Schröder, D. C. Langreth, and B. I. Lundqvist, Van der Waals Density Functional for General Geometries, Phys. Rev. Lett. **92**, 246401 (2004).

[40] J. Klimeš, D. R. Bowler, and A. Michaelides, Van der Waals density functionals applied to solids, Phys. Rev. B **83**, 195131 (2011).

[41] J. Hong, Z. Hu, M. Probert, K. Li, D. Lv, X. Yang, L. Gu, N. Mao, Q. Feng, and L. Xie *et al.*, Exploring atomic defects in molybdenum disulphide monolayers, Nat. Commun. **6**, 6293 (2015).

[42] S. N. Steinmann and C. Corminboeuf, A generalized-gradient approximation exchange hole model for dispersion coefficients, J. Chem. Phys. **134**, 044117 (2011).

[43] S. N. Steinmann and C. Corminboeuf, Comprehensive benchmarking of a density-dependent dispersion correction, J. Chem. Theory Comput. **7**, 3567 (2011).

[44] J. P. Perdew, K. Burke, and M. Ernzerhof, Generalized Gradient Approximation Made Simple, Phys. Rev. Lett. **77**, 3865 (1996).

[45] J. Heyd, G. E. Scuseria, and M. Ernzerhof, Hybrid functionals based on a screened Coulomb potential, J. Chem. Phys. **118**, 8207 (2003).

[46] J. Heyd, G. E. Scuseria, and M. Ernzerhof, Erratum: "Hybrid functionals based on a screened Coulomb potential", J. Chem. Phys. **124**, 219906 (2006).

[47] S. Grimme, J. Antony, S. Ehrlich, and H. Krieg, A consistent and accurate ab initio parametrization of density functional dispersion correction (DFT-D) for the 94 elements H-Pu, J. Chem. Phys. **132**, 154104 (2010).

[48] M. Cococcioni and S. de Gironcoli, Linear response approach to the calculation of the effective interaction parameters in the LDA+U method, Phys. Rev. B **71**, 035105 (2005).

[49] T. Li, S. Jiang, N. Sivadas, Z. Wang, Y. Xu, D. Weber, J. E. Goldberger, K. Watanabe, T. Taniguchi, and C. J. Fennie *et al.*, Pressure-controlled interlayer magnetism in atomically thin CrI3, Nat. Mater. **18**, 1303 (2019).

[50] T. Song, Z. Fei, M. Yankowitz, Z. Lin, Q. Jiang, K. Hwangbo, Q. Zhang, B. Sun, T. Taniguchi, and K. Watanabe *et al.*, Switching 2D magnetic states via pressure tuning of layer stacking, Nat. Mater. **18**, 1298 (2019).

[51] Y. Mokrousov, G. Bihlmayer, S. Blügel, and S. Heinze, Magnetic order and exchange interactions in monoatomic 3*d* transition-metal chains, Phys. Rev. B **75**, 104413 (2007).

[52] S. Khmelevskyi and P. Mohn, Relationship between magnetic and structural properties of Ni thin films on GaAs(100) and bulk bcc Ni: First-principles calculations, Phys. Rev. B **75**, 012411 (2007).

[53] S. Morán, C. Ederer, and M. Fähnle, Ab initio electron theory for magnetism in Fe: Pressure dependence of spin-wave energies, exchange parameters, and Curie temperature, Phys. Rev. B **67**, 012407 (2003).

[54] L. Gross, F. Mohn, N. Moll, P. Liljeroth, and G. Meyer, The chemical structure of a molecule resolved by atomic force microscopy, Science **325**, 1110 (2009).

[55] J. Zhang, P. Chen, B. Yuan, W. Ji, Z. Cheng, and X. Qiu, Real-space identification of intermolecular bonding with atomic force microscopy, Science **342**, 611 (2013).

[56] K.-A. N. Duerloo, Y. Li, and E. J. Reed, Structural phase transitions in two-dimensional Mo- and W-dichalcogenide monolayers, Nat. Commun. **5**, 4214 (2014).

[57] X. Qian, J. Liu, L. Fu, and J. Li, Quantum spin Hall effect in two-dimensional transition metal dichalcogenides, Science **346**, 1344 (2014).

[58] D. H. Keum, S. Cho, J. H. Kim, D.-H. Choe, H.-J. Sung, M. Kan, H. Kang, J.-Y. Hwang, S. W. Kim, and H. Yang *et al.*, Bandgap opening in few-layered monoclinic $MoTe_2$, Nat. Phys. **11**, 482 (2015).

[59] S. Tang, C. Zhang, D. Wong, Z. Pedramrazi, H.-Z. Tsai, C. Jia, B. Moritz, M. Claassen, H. Ryu, and S. Kahn *et al.*, Quantum spin Hall state in monolayer 1T'-WTe_2, Nat. Phys. **13**, 683 (2017).

[60] A. Nakamura, T. Shimojima, M. Matsuura, Y. Chiashi, M. Kamitani, H. Sakai, S. Ishiwata, H. Li, A. Oshiyama, and K. Ishizaka, Evaluation of photo-induced shear strain in monoclinic VTe_2 by ultrafast electron diffraction, Appl. Phys. Express **11**, 092601 (2018).

[61] M. Kan, S. Adhikari, and Q. Sun, Ferromagnetism in MnX_2 (X = S, Se) monolayers, Phys. Chem. Chem. Phys. **16**, 4990 (2014).

[62] Y. Shi, Y. Guo, S. Yu, M. Arai, A. Sato, A. A. Belik, K. Yamaura, and E. Takayama-Muromachi, Crystal growth and structure and magnetic properties of the 5d oxide Ca_3LiOsO_6: Extended superexchange magnetic interaction in oxide, J. Am. Chem. Soc. **132**, 8474 (2010).